



This is a repository copy of *Relative periodic solutions in conducting liquid films flowing down vertical fibres*.

White Rose Research Online URL for this paper:  
<http://eprints.whiterose.ac.uk/146668/>

Version: Accepted Version

---

**Article:**

Ding, Z. and Willis, A. [orcid.org/0000-0002-2693-2952](https://orcid.org/0000-0002-2693-2952) (2019) Relative periodic solutions in conducting liquid films flowing down vertical fibres. *Journal of Fluid Mechanics*, 873. pp. 835-855. ISSN 0022-1120

<https://doi.org/10.1017/jfm.2019.450>

---

This article has been published in a revised form in *Journal of Fluid Mechanics* [<http://doi.org/10.1017/jfm.2019.450>]. Article available under the terms of the CC-BY-NC-ND license (<https://creativecommons.org/licenses/by-nc-nd/4.0/>). © Cambridge University Press.

**Reuse**

This article is distributed under the terms of the Creative Commons Attribution-NonCommercial-NoDerivs (CC BY-NC-ND) licence. This licence only allows you to download this work and share it with others as long as you credit the authors, but you can't change the article in any way or use it commercially. More information and the full terms of the licence here: <https://creativecommons.org/licenses/>

**Takedown**

If you consider content in White Rose Research Online to be in breach of UK law, please notify us by emailing [eprints@whiterose.ac.uk](mailto:eprints@whiterose.ac.uk) including the URL of the record and the reason for the withdrawal request.



[eprints@whiterose.ac.uk](mailto:eprints@whiterose.ac.uk)  
<https://eprints.whiterose.ac.uk/>

# Relative periodic solutions in conducting liquid films flowing down vertical fibres

Zijing Ding<sup>1†</sup> and Ashley P. Willis<sup>2‡</sup>

<sup>1</sup>Department of applied mathematics and theoretical physics, University of Cambridge, UK.

<sup>2</sup>School of Mathematics and Statistics, University of Sheffield, UK.

(Received ?; revised ?; accepted ?.)

The dynamics of a conducting liquid film flowing down a cylindrical fibre, subjected to a radial electric field, is investigated using a long-wave model (Ding et al. *JFM* **752**, 2014). In this study, to account for the complicated interactions between droplets, we consider two large droplets in a periodic computational domain and find two distinct types of travelling wave solutions, which consist of either two identical (type-I) or two slightly different droplets (type-II). Both are ‘relative’ equilibria, i.e. steady in a frame moving at their phase speed, and are stable in smaller domains when the electric field is weak. We also study relative periodic orbits, i.e. temporally recurrent dynamic solutions of the system. In the presence of the electric field, we show how these invariant solutions are linked to the dynamics, where the system can evolve into either, one of the steady travelling wave states, an oscillatory state, or a “singular-structure” (Wray et al. *JFM* **735**, 2013; Ding et al. *JFM* **752**, 2014). We find that the oscillation between two similarly-sized large droplets in the oscillatory state is well represented by relative periodic orbits. Varying the electric field strength, we demonstrate that relative periodic solutions arise as the dynamically important solution once the type-I or type-II travelling wave solutions lose stability. Oscillation can be either enhanced or impeded as the electric field’s strength increases. When the electric field is strong, no relative periodic solutions are found and a spike-like singular structure is observed. For the case where the the electric field is not present, the oscillation is instead caused by the interaction between a large droplet and a nearby much smaller droplet. We show that this oscillation phenomenon originates from the instability of the type-I travelling wave solution in larger domains, and that the oscillatory state can again be represented by an exact relative periodic orbit. The relative periodic orbit solution is also compared with experimental study for this case. The present study demonstrates that the relative periodic solutions are better at capturing the wave speed and oscillatory dynamics than the travelling wave solutions in the unsteady flow regime.

**Key words:** Liquid film, Relative periodic solution, Electric field

---

## 1. Introduction

Over the past few decades, due to the vast number of applications in coating technology, liquid film flows have received much attention. Many experimental and theoretical works have focused on a liquid film flowing down a flat plane (Oron, Davis & Bankoff

† z.ding@damtp.cam.ac.uk

‡ a.p.willis@sheffield.ac.uk

1997; Craster & Matar 2009) and a cylindrical surface (Quéré 1999). A liquid film coating a cylindrical surface has potential applications in oil recovery and biological flows, particularly in connection with the drawing of fibres from liquid baths. The well-known Plateau-Rayleigh mechanism modulated by the gravity driven flow gives rise to many interesting dynamical phenomena, e.g. organized sliding beads and the breakup of liquid films, which have attracted much experimental and theoretical attention (De Ryck & Quéré 1996; Duprat *et al.* 2007; Ruyer-Quil *et al.* 2008; Duprat *et al.* 2009).

To investigate the dynamics of a liquid film coating the exterior surface of a vertical fibre at low Reynolds number, most theoretical works have employed a reduced-order model. Pioneering work on a very thin film was carried out by Frenkel (1992), who derived a thin film model and showed that the liquid film is linearly unstable due to azimuthal curvature. The nonlinear dynamics of the thin film model has been examined to account for droplet formation by Kalliadasis & Chang (1994); Chang & Demekhin (1999). Kliakhandler *et al.* (2001) investigated a much thicker film, where the thin film model can no longer be applied, and observed three different flow regimes, labelled “a”, “b” and “c”. In flow regime “a”, where the flow rate is high ( $\sim 22\text{mm}^3/\text{s}$ ), large droplets maintain their shape, travel at a constant speed and are separated by a flat film. At moderate flow rates ( $\sim 11\text{mm}^3/\text{s}$ ), flow regime “b” labels a necklace-like structure, i.e. close and regularly spaced droplets. Flow regime “c” corresponds to an oscillatory state observed at low flow rates ( $\sim 5\text{mm}^3/\text{s}$ ), in which a big droplet coexists with several small beads. The large droplet catches up with and consumes small beads at its front, before breaking up into small beads at its rear. The thick film model retaining the full surface curvature proposed by Kliakhandler *et al.* (2001) failed to find a solution similar to flow regime “a” in numerical simulations. Craster & Matar (2006) reduced the curvature asymptotically and showed that the travelling wave solutions of the asymptotic model captures the correct wave speed of flow regime “a”. Neither the thick film model nor the asymptotic model, however, capture the wave speed of the necklace-like structure in flow regime “b”. This perhaps is because the long-wave assumption of the reduced-order models does not hold in flow regime “b”. The flow regime “c” is not steady but oscillates due to the droplet coalescence and breakup process. Recent experimental studies of flow regime “c” have confirmed that it is a time-periodic state (Sadeghpour, Zeng & Ju 2017; Zeng *et al.* 2017). In most previous studies, steady travelling wave solutions have been computed and compared with the flow regime “c” (Craster & Matar 2006; Ruyer-Quil *et al.* 2008; Novbari & Oron 2009). However, it is questionable whether or not a travelling wave solution should be used to compare with the oscillating flow regime “c”, when one is steady and the other is unsteady. It is natural to ask whether there is an unsteady solution, i.e. a relative periodic orbit solution, that can not only capture the dynamics of the oscillation, but also the wave speed of flow regime “c”.

When inertial effects are taken into account, two coupled equations governing the film thickness and the flow rate can be derived, such as the integral-boundary-layer model (Trifonov 1992; Sisoiev *et al.* 2006; Shkadov *et al.* 2008), energy integral model (Novbari & Oron 2009) and the weighted-residual model (Ruyer-Quil *et al.* 2008). A short-coming of the integral boundary layer model is that it fails to predict the correct linear stability of a film flowing down a moderately tilted plane, which can be addressed by the weighted residual model (Ruyer-Quil & Manneville 1998). The energy integral model and the weighted-residual model are more accurate than the thick film model and the asymptotic model. For instance, a small capillary ripple in front of the big droplet predicted by the asymptotic model is not obvious in experiment, but is eliminated in the weighted-residual model (Ruyer-Quil *et al.* 2008). Pradas, Tseluiko & Kalliadasis (2011), however, has shown that this small capillary ripple can have an important effect on the formation of

bound states, which consist of several different-sized pulses moving together. The bound states can be either steady or oscillatory (Pradas, Tseluiko & Kalliadasis 2011). Very recently, Blyth *et al.* (2018) showed that there are countably infinite sets of bound states in an electrified liquid film flowing down an inclined plane.

For industrial applications, it is interesting to design an active control method to modify the interfacial instability to induce pattern formation. The application of an electric field has been a successful candidate for this purpose (Papageorgiou 2018), e.g. using an electric field to control pattern formation in a liquid film on a flat plane (Schäffer *et al.* 2000; Craster & Matar 2005) and droplet production from liquid jets (Wang *et al.* 2011; Conroy *et al.* 2011). The idea of using an electric field was also transplanted into the control of instability of liquid film flows on vertical fibres (Wray *et al.* 2012, 2013a,b; Ding *et al.* 2014; Liu, Chen & Ding 2018). The asymptotic model was used to investigate the dynamics of the electrified films (Wray *et al.* 2012, 2013a,b; Ding *et al.* 2014; Liu, Chen & Ding 2018). Recently, other control methods, e.g., varying the nozzle size (Sadeghpour, Zeng & Ju 2017) or using a countercurrent gas flow (Zeng *et al.* 2017), have been used to modulate the pattern formation in liquid films on vertical fibres.

When the liquid is a leaky dielectric, the electric field can suppress the Plateau-Rayleigh instability or attract the liquid to the electrode, leading to the ‘touch-down’ structure (Wray *et al.* 2012, 2013a,b), where the liquid interface is attracted to the fibre (the inner electrode). When the liquid is perfectly conducting, instead, a spike-like structure is observed (Ding *et al.* 2014; Liu, Chen & Ding 2018), where the liquid interface touches the outer electrode. Self-similarity analysis has shown that the minimal film thickness in touch-down state scales as  $(\Delta t)^{1/3}$  (Wray *et al.* 2013a), and the spike-like structure develops as  $(\Delta t)^{1/6}$  ( $\Delta t = t_s - t$  with singularity formation time  $t_s$ ) (Liu, Chen & Ding 2018). The interested reader may consult the review paper by Saville (1997) for more details on the dielectric models of liquids. When the electric field was not strong, both a saturated travelling wave state and an oscillatory state were observed in these studies. The oscillation can either be periodic or chaotic in the presence of an electric field. Further, the oscillation between large droplets that are close in size can occur.

Oscillatory behaviour is different in non-electrified film flow (Ding *et al.* 2014), where oscillations occur only through the interaction between a large droplet and a much smaller droplet. The travelling wave solution for a single droplet shows that a large droplet moves faster than a small droplet, and therefore a conclusion of the theoretical study is that a big droplet catches up with, and consumes, a smaller droplet. The resulting bigger droplet can be unstable, breaking up into smaller droplets, leading to an oscillatory or chaotic state (Craster & Matar 2006; Ding & Wong 2017). Travelling wave solutions of a non-electrified film flow of slightly different sized droplets can move as a bound state (Trifonov 1992; Sisoiev *et al.* 2006; Ruyer-Quil & Manneville 1998), which do not exhibit oscillation. Moreover, experimental study of a non-electrified film has also shown that slightly different-sized droplets can also move in a stable bound state (Duprat *et al.* 2007). These theoretical and experimental studies imply that oscillation is unlikely to occur through the interactions between large droplets, without the help of an electric field. A minor point to address, however, is that it is not clear how the electric field induces the oscillation between large droplets in the electrified film flow on a vertical cylinder. A related question is how the oscillation influences the wave speed. Does the oscillation accelerate or slow down the motion of droplets? A quick answer to this question can be found in figure 4(b-d), where in general it is seen that the oscillation slows down the droplet.

Travelling wave solutions cannot provide a full understanding of the dynamics of a liquid film flowing down a vertical cylinder, in particular, the oscillatory phenomenon. From

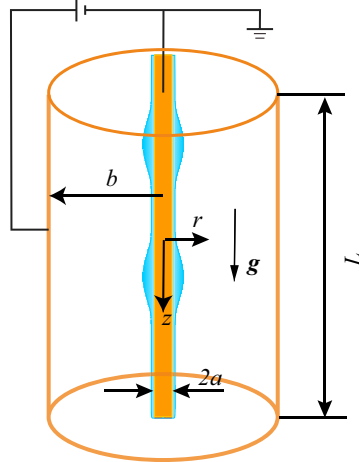


FIGURE 1. Geometry of the system. The mean radius of the liquid film is  $h_0$ .

the viewpoint of dynamical systems theory, travelling wave solutions are called ‘relative’ equilibria of the phase space. Their integral properties are constant and do not capture the dynamics of unsteady flows. Travelling waves, however, can be unstable to a Hopf bifurcation, leading to the emergence of relative periodic orbits (Cvitanović, Davidchack & Siminos 2010; Chantry, Willis & Kerswell 2014). These ‘relative’ periodic orbits are periodic orbits in a frame with non-zero phase speed. (A periodic orbit of the original system must have exactly zero phase shift after one period, but the probability of such a shift is zero for a homogeneous system, unless the solution carries a reflectional symmetry.) Indeed, relative period orbits are thought of as the building blocks of a chaotic attractor in turbulent flows, e.g. turbulent Couette flow (Viswanath 2007), Kolmogorov flow (Chandler & Kerswell 2013) and pipe flow (Budanur *et al.* 2017). This paper is therefore inspired by recent research in transitional turbulence. We aim to explore relative periodic solutions in liquid film flows down a vertical fibre. In contrast to steady travelling wave solutions, we believe that relative periodic solutions should provide a better understanding of the oscillatory dynamics of the electrified film, and in particular, the regime “c” of non-electrified flow.

A synopsis of this paper is as follows. §2 formulates the problem and a long-wave model is derived. Numerical methods for extracting steady travelling wave and relative periodic solutions are provided in §3. The oscillation caused by electric field is discussed in §4.1, which is followed by a discussion of oscillation in an non-electrified film in §4.2. A conclusion is made in §5.

## 2. Mathematical formulation

We consider an axisymmetric perfectly-conducting liquid film of constant density  $\rho$  and dynamic viscosity  $\mu$ . The flow down a vertical fibre, modelled by a cylinder, is driven by gravity  $g$  and subjected to a radial electric field (see figure 1). The annular flow system is enclosed in a co-axial cylindrical electrode. A high electric voltage  $\phi_0$  is applied at the outer electrode, while the central metal fibre is grounded. Throughout this paper, the surrounding dielectric gas is considered to be inviscid and its dynamics is therefore neglected. The outer cylinder cannot be neglected, however, as it is required to impose a uniform electric field.

We assume that the mean radius to the surface of the fluid ring  $h_0$  is much smaller than

its characteristic length  $\mathcal{L}$  in the axial direction and define a small parameter  $\epsilon = h_0/\mathcal{L}$ . Craster & Matar (2006) took the length scale  $\mathcal{L}$  to be related to the capillary length:  $\mathcal{L} = \gamma/\rho g h_0$ , so that the dimensionless equations would not rely on the fluid thickness being small relative to the fiber radius, but instead small relative to a dynamic length scale. The small parameter is then  $\epsilon = \rho g h_0^2/\gamma$ , which is also known as the Bond number  $Bo$ , and in experiment is typically small,  $Bo \sim 0.3$  or so (Craster & Matar 2006). We non-dimensionalize the system by introducing the length scales  $r = h_0 r'$ ,  $z = \mathcal{L} z'$ , pressure scale  $p - p_g = \rho g \mathcal{L} p'$ , electric potential  $\phi = \phi_0$ , velocity scales  $w = W w'$ ,  $u = \epsilon W u'$ ,  $t = \mathcal{L}/W t'$  ( $W = \rho h_0^2 g/\mu$ ,  $p_g$  is the pressure of the gas phase). This paper considers the leading order dynamics, and the evolution equation of the interfacial shape  $h(z, t)$  derived by Ding *et al.* (2014) is adopted:

$$h_t + \frac{1}{h} \left[ \frac{1-p_z}{4} \left( h^4 \ln \left( \frac{h}{\alpha} \right) + \frac{(\alpha^2 - h^2)(3h^2 - \alpha^2)}{4} \right) \right]_z = 0, \quad (2.1)$$

where  $p = -E_b \phi_r^2/2 + 1/h - \epsilon^2 h_{zz}$  and the electrostatic force  $\phi_r^2 = h^{-2}[\ln(h/\beta)]^{-2}$  at the leading order approximation. The dimensionless radii are  $\alpha = a/h_0$  and  $\beta = b/h_0$ .  $E_b = \epsilon \epsilon \phi_0^2/\rho g h_0^3$  is the electric Weber number and  $\epsilon$  the electric permittivity. When the electric field is turned off, (2.1) reduces to the model of Craster & Matar (2006) immediately.

In this paper, to seek for the recurrent solutions, i.e. relative equilibria (travelling waves) and relative periodic orbits, we solve for the local cross-sectional area  $S = h^2$  rather than the liquid radius  $h$ :

$$S_t + 2 \left( (1-p_z) \left[ \frac{S^2}{4} \ln \left( \frac{S^{1/2}}{\alpha} \right) + \frac{(3S - \alpha^2)(\alpha^2 - S)}{16} \right] \right)_z = 0 \quad (2.2)$$

where

$$p = \frac{1}{S^{1/2}} - \epsilon^2 \left( \frac{1}{2} S^{-1/2} S_{zz} - \frac{1}{4} S^{-3/2} S_z^2 \right) - \frac{E_b}{2} S^{-1} \left( \frac{1}{2} \ln S - \ln \beta \right)^{-2}.$$

It follows from mass conservation that  $S$  is temporally conserved:

$$\langle S \rangle = \frac{1}{L} \int_0^L S dz = 1, \quad (2.3)$$

where  $L$  is the axial length of the domain. The equations for  $S$  are numerically more convenient than those for  $h$ : when using a Newton method to update  $S$ , where  $S$  is expressed as a Fourier expansion, the mean mode is fixed by the constraint (2.3), while changes to the coefficients of the other modes do not affect (2.3).

For visualisation purposes, we introduce an energy-like norm  $\mathcal{E} = \langle S^2/2 \rangle$ . Then, the energy balance in the system is

$$\dot{\mathcal{E}} = \mathcal{I} - \mathcal{D}, \quad (2.4)$$

where

$$\begin{aligned} \mathcal{I} &= \frac{1}{2} \left\langle S^{-3/2} S_z^2 Q \right\rangle, \\ \mathcal{D} &= \left\langle \epsilon^2 \left( \frac{1}{2} S^{-1/2} S_z S_{zzz} + \frac{3}{8} S^{-5/2} S_z^4 - \frac{3}{4} S^{-3/2} S_{zz} S_z^2 \right) Q \right\rangle \\ &\quad + \left\langle E_b/2 S^{-1} \left( \frac{1}{2} \ln S - \ln \beta \right)^{-2} S_z Q \right\rangle_z, \end{aligned}$$

with  $Q = S^2 \ln(S^{1/2}/\alpha)/4 + (3S - \alpha^2)(\alpha^2 - S)/16$ . We will project the solution onto the energy production  $\mathcal{I}$  and energy dissipation  $\mathcal{D}$  plane. For travelling waves (hereafter TWs), the dissipation equals the production  $\mathcal{D} = \mathcal{I}$ ; and for relative periodic orbits (hereafter, referred to as RPOs), the orbits in the  $\mathcal{I}$  vs.  $\mathcal{D}$  are closed loops with a temporal average centered on  $\mathcal{D} = \mathcal{I}$ .

### 3. Recurrent solutions: dynamical systems approach

Recurrent solutions of the dynamical system (2.2) satisfy

$$S(z + l, t + T) = S(z, t), \quad (3.1)$$

where  $l$  is a spatial shift along the axis of the fibre and  $T$  is a period. Each relative periodic orbit (RPO) has its particular period  $T$ , while for a travelling wave (TW) the period  $T$  may be freely chosen, and the shift is related to the phase speed by  $c = l/T$ . If  $T$  is large, then we may need to account for the periodicity,  $c = (l + nL)/T$ , where  $n$  is an integer. For an RPO solution, we use a  $\bar{c}$  to represent its mean speed.

The solution of Eq.(2.2) is approximated by a Fourier expansion:

$$S(z, t) = \sum_{j=-N+1}^N \hat{S}_j(t) \exp\left(ij \frac{2\pi}{L} z\right). \quad (3.2)$$

Derivatives in  $z$  are computed in the Fourier space, and nonlinear terms are evaluated on a uniform grid in real space. For the calculations of this paper we have used 256 – 320 Fourier modes. An implicit Gear's method in time is implemented, and the error after  $T/\Delta t$  timesteps of size  $\Delta t$  is less than  $10^{-6}$  relative to the solution for  $\Delta t \rightarrow 0$  (Ding *et al.* 2014).

Given an initial guess  $(S_0, l, T)$ , using Newton's method to find a root of  $(S - S_0)$ , where  $S = S(z + l, t + T)$  and  $S_0 = S(z, t)$ , a better guess  $(S_0 + \delta S_0, l + \delta l, T + \delta T)$  is given by

$$\frac{\partial S}{\partial S_0} \delta S_0 + \frac{\partial S}{\partial l} \delta l + \frac{\partial S}{\partial T} \delta T - \delta S_0 = -(S - S_0). \quad (3.3)$$

As there are  $2N + 2$  unknowns  $\delta S_0$ ,  $\delta l$  and  $\delta T$ , we need two more constraints to close the system. We impose that  $\delta S_0$  has no component that shifts the solution in the  $z$  direction or the  $t$  direction (Viswanath 2007),

$$\delta S_0 \frac{\partial S_0}{\partial z} = 0, \quad (3.4)$$

$$\delta S_0 \frac{\partial S_0}{\partial t} = 0. \quad (3.5)$$

For TWs we drop the second condition in (3.5) and we take  $T$  fixed. Equations (3.3), (3.4), (3.5) constitute the following system:

$$\mathcal{A} \mathbf{x} = \mathbf{b}, \quad (3.6)$$

where  $\mathbf{x} = (\delta S_0, \delta l, \delta T)$  and  $\mathbf{b} = (S - S_0, 0, 0)$ . The system (3.6) can be solved using the GMRES method, which approximates the solution in the Krylov subspace spanned by  $\mathcal{K}_m = \{\mathbf{b}, \mathcal{A}\mathbf{b}, \mathcal{A}^2\mathbf{b}, \dots, \mathcal{A}^{m-1}\mathbf{b}\}$ . Typically  $\mathcal{K}_m$  is small,  $m = O(10)$ . To evaluate the result of multiplication by the Jacobian, we use the approximation

$$\frac{\partial S}{\partial S_0} \delta S_0 \approx \frac{S(z, T; S_0 + e \delta S_0) - S(z, T; S_0)}{e}, \quad (3.7)$$

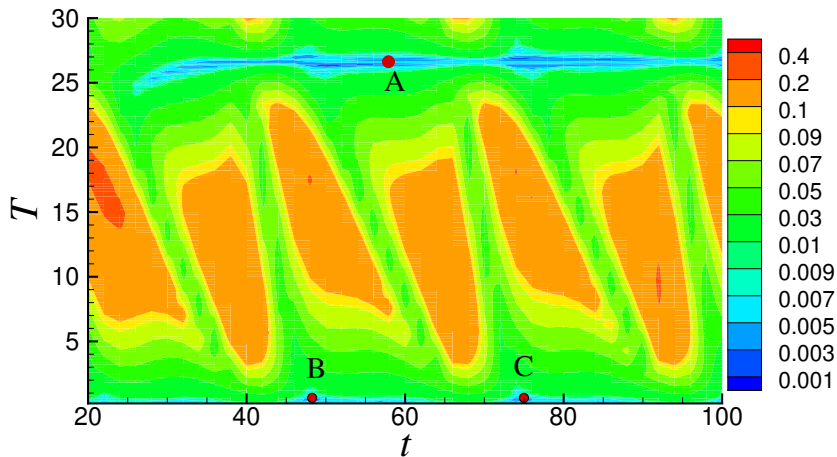


FIGURE 2. Example of  $R_d(t, T)$  at  $E_b = 2$  and  $L = 4$  contoured over  $t \in [20, 100]$  and  $T \in [0.2, 30]$ . Minimal value of  $R_d \sim 10^{-3}$  is found near  $T = 26$ . The three marked points, labeled A, B, C, are used as initial guesses for the Newton–Krylov iteration, and only point A converges.

wherein  $e$  is an empirical small parameter. We set  $e$  such that  $e \|\delta S_0\|/\|S_0\| = 10^{-4}$ . We terminate the GMRES iterations when  $\|\mathcal{A}\mathbf{x} - \mathbf{b}\|/\|\mathbf{b}\| \leq 10^{-3}$ . For the Newton step, the iteration is terminated when  $\|S - S_0\|/\|S_0\| < 10^{-6}$  and typically the relative error is  $O(10^{-8})$  for the solutions presented in this paper. Failure of Newton method is commonplace when the initial guess is not good enough. To improve the domain of convergence, we applied a “hook-step” to move  $(\delta S_0, \delta l, \delta T)$  within a trust region. For more information on the numerical method, excellent descriptions of the Newton–Krylov-hookstep method can be found in Viswanath (2007); Chandler & Kerswell (2013). The Newton–Krylov code is validated by recomputing the TW solutions by a direct Newton code of Ding *et al.* (2014) (see figure 4).

An good initial guess for the Newton–Krylov code is required in order to stand a good change of convergence to solution. In this paper, we follow Cvitanović & Gibson (2010) and search for near recurrences by calculating normalized difference between states, namely  $R_d(t, T)$ , which is minimized over continuous shift in  $z$  direction, after each interval of  $t = 0.1$  or  $t = 0.2$ :

$$R_d(t, T) = \min_{0 \leq l \leq L} \frac{\|S(t+T, z+l) - S(t, z)\|}{\|S(t, z)\|}. \quad (3.8)$$

We consider cases where  $R_d < 10^{-2}$  as candidates. Figure 2 illustrates a good initial guess at around  $40 < t < 100$  with  $T \approx 26$ . A snapshot of  $S(z, t)$  taken from “A” was used as an initial guess and converged to an RPO discussed in §4.1. Once an RPO is obtained, we used parametric continuation to track solutions.

#### 4. Results and discussion

In the following discussions, we first explore RPOs in an electrified film in §4.1, which aims at providing insight into the oscillation caused by interactions between two big droplets. When the electric field is turned off, however, interactions between big droplets do not cause an oscillatory flow. Instead, oscillation is due the complicated interaction between a large droplet and a much smaller droplet. And we will demonstrate this os-

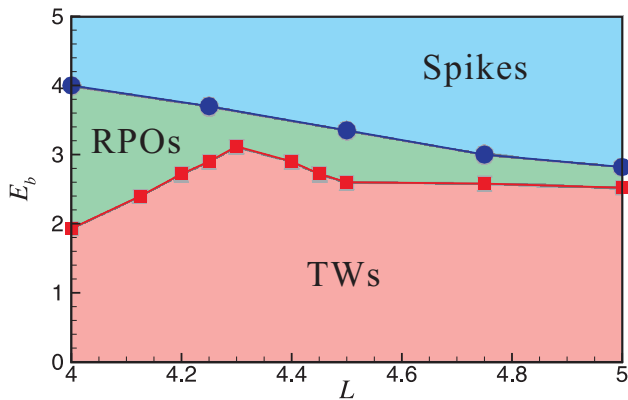


FIGURE 3. Phase diagram of solution regimes in the  $L$  vs.  $E_b$  plane. The boundaries separating different solution regimes are obtained starting from RPOs and tracking where they undergo transition to spikes or TWs.

cillation caused by a large droplet and a small droplet can be represented by an RPO in §4.2. In particular, the flow regime “c” in the experimental study (Kliakhandler *et al.* 2001) is compared with an RPO solution.

#### 4.1. Invariant solutions in an electrified film

This section examines the oscillatory phenomenon in an electrified film. Previous numerical simulations have shown that an oscillation between big droplets can occur when subjected to an electric field (Wray *et al.* 2013a; Ding *et al.* 2014). Stability analysis of a uniform film,  $S = 1$ , has shown that for  $\beta < \exp(1)$  the electric field can enhance the linear instability. For  $\beta > \exp(1)$ , however, the electric field impedes the linear instability, but is destabilising with respect to finite amplitude perturbations. The flow then proceeds to the formation of an oscillatory state or spike-like singular state, dependent on the value of  $\beta$  (Ding *et al.* 2014). In this paper, we are interested in the oscillatory state and therefore fix the radius of the outer electrode at  $\beta = \exp(1.1)$ . In the following discussion, we fix the small parameter  $\epsilon$ , and the radius of the fibre  $\alpha$  at  $(\epsilon, \alpha) = (0.2, 0.25)$  following previous studies, e.g. Craster & Matar (2006); Liu, Chen & Ding (2018). To understand the oscillation dynamics between big droplets, we consider a periodic computational domain that is large enough for two big droplets. To determine an appropriate domain size  $L$ , we refer to the linear stability analysis by Ding *et al.* (2014), where the wave length of the most unstable mode in the electrified film is

$$\frac{2\sqrt{2}\epsilon\pi}{\sqrt{1 + \frac{E_b(1-\ln(\beta))}{\ln^3(\beta)}}} \sim 2. \quad (4.1)$$

We therefore start with domain sizes of  $L \sim 4$  for  $0 \leq E_b \leq 4$  to allow two big droplets. Figure 3 shows the type of solution observed in simulations for the range  $4 \leq L \leq 5$ . For  $L > 6$ , we expect three or more big droplets to form in the domain.

Initially, to find stable states in simulations, we perturb the trivial solution  $S = 1$  by harmonic waves

$$S(z, 0) = 1 + 0.1 \cos\left(n \frac{2\pi}{L} z\right), \quad (4.2)$$

with  $n = 1$  or  $n = 2$  and with  $E_b$  small. For  $L = 4$ , we find that the system evolves

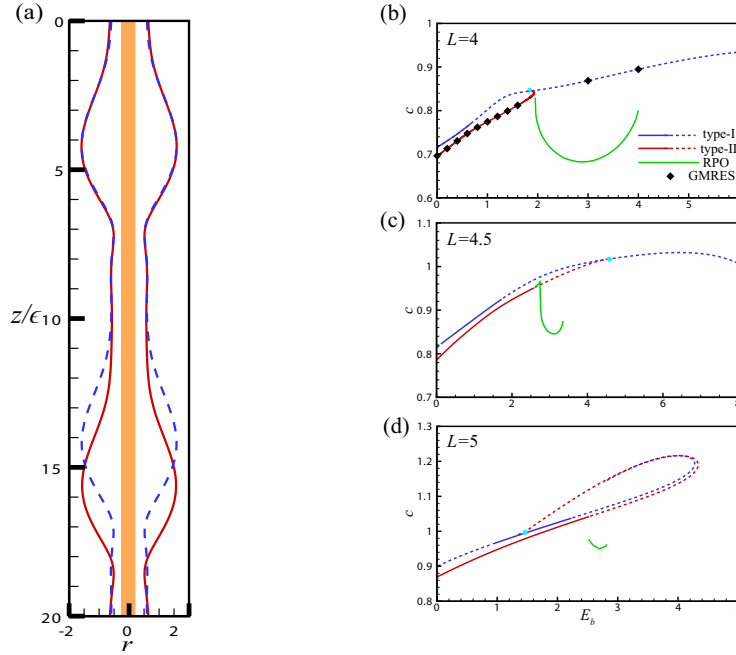


FIGURE 4. (a) The profiles of the “two different/identical droplets” (type-I/type-II) illustrated by “blue/red” lines for  $E_b = 1$ ,  $L = 4$ . (b-d) The wave speed  $c$  vs. the electric number  $E_b$  for  $L = 4, 4.5, 5$  respectively. The type-I TW branch for  $L = 5$  stops at  $E_b = 2.76$  after turns back, as the singular structure appears. Curves for TWs are obtained by a direct Newton–Raphson iteration using the code of Ding *et al.* (2014). Curves for RPOs in (b-d) are obtained from the Newton–Krylov method implemented in this work. Stable/unstable TW branches are solid/dashed lines. The Newton–Krylov method is validated by re-producing the TW solution as marked by diamonds in (b). The bullets indicates where the type-II TW connects with type-I TW.

into one of two stable TW states. For  $n = 2$ , two identical droplets form, hereafter called type-I. Their spatial period is  $L/2$ , but they are stable to small disturbances of  $n = 1$  type. Starting with  $n = 1$  in (4.2), two slightly different droplets form, hereafter referred to as type-II. The two forms of TW solution are illustrated in figure 4(a). Starting from these non-oscillatory solutions at  $L = 4$ ,  $E_b = 0$ , pseudo-arclength continuation with the code of Ding *et al.* (2014) has been used to track the TW solutions and the wave speed  $c$  against the electric Weber number  $E_b$ , shown in figure 4(b-d). For the case of type-II TW, the  $c$  vs.  $E_b$  curve is shown in figure 4(b), which folds back at  $E_b \approx 1.94$  for  $L = 4$ , while the curve stops at around  $E_b = 4.3$  for  $L = 4.5$ . Thus, for both  $L = 4$  and  $L = 4.5$  this indicates that the type-II TWs do not exist when the electric field exceeds some critical value. For  $L = 5$  neither type of solution exists for  $E_b \gtrsim 4$ .

Numerical simulations of TW solutions show that they lose stability to an oscillatory bound state when  $E_b$  exceeds a critical value. (See figure 5(a)). The oscillation suggests the existence of RPOs, which will be discussed presently. For larger  $E_b$ , we observe that two droplets start to merge, and the minimal gap between the liquid interface and outer electrode reduces quickly — Ding *et al.* (2014) showed that the outer electrode attracts the interface, and the liquid interface becomes unstable. It is quickly attracted to the outer electrode when the gap is small, leading to the formation of the spike-like structure. (An example of the spike-like structure can be found in figure 5(b).) It

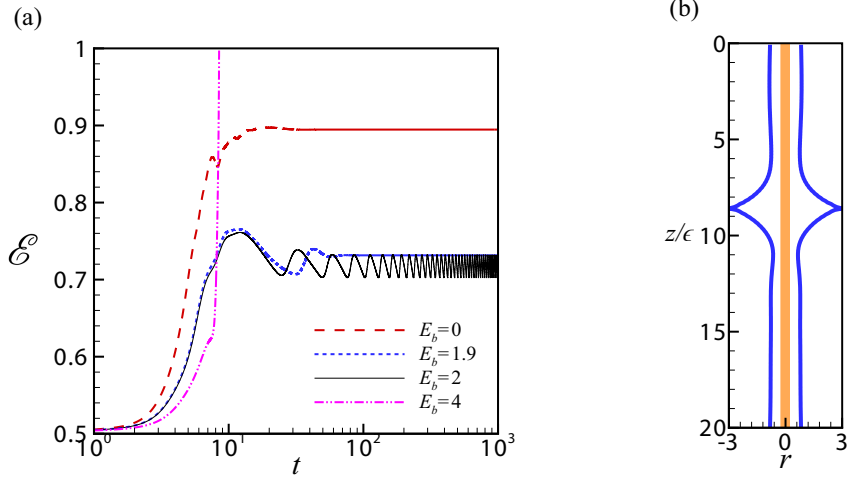


FIGURE 5. (a) Evolution of the energy norm  $\mathcal{E} = \langle S^2/2 \rangle$  at different electric number subject to the initial condition  $S(z, 0) = 1 + 0.1 \cos(\pi z/2)$  where  $z \in [0, 4]$ . For  $E_b = 0, 1.9$ , steady type-II TWs are obtained (see that  $\mathcal{E}$  becomes invariant). (b) The spike-like structure plotted at  $t \approx 8.5$  at  $E_b = 4, L = 4$ .

is natural to examine whether the oscillatory solutions are linked to the TW solutions through oscillatory bifurcations.

The two leading eigenvalues (either two real or a complex pair) of the type-I TWs are plotted against  $E_b$  in figure 6 for (a,b)  $L = 4$ , (c,d)  $L = 4.5$  and (e,f)  $L = 5$ . The eigenvalues for the type-II TW for these parameters are shown in figure 7.

At  $L = 4$  the type-I TW becomes unstable when  $E_b > 0.66$ , but the unstable mode is not oscillatory until  $E_b \gtrsim 1.94$ . Numerical simulation show that type-I TWs lose stability and evolve into type-II TWs for  $0.66 < E_b < 1.94$ , and the type-II TWs is stable over this range. For  $E_b > 1.94$  the dynamics develop into an RPO.

For  $L = 4.5$ , figures 6(c,d) show that the oscillatory eigenmode is always stable, and the unstable mode is always real. In this case, RPOs do not originate from the instability of type-I TWs, but instead comes from the instability of type-II TWs when  $E_b > 2.6$  as demonstrated by figure 7(a). Figure 4(c) shows that the RPO branch connects with the type-II TW branch.

For  $L = 5$ , type-I TWs are unstable to a real mode when  $E_b < 0.92$  or  $E_b > 3.92$  while the mode is unstable and oscillatory for  $2.23 < E_b < 3.92$ . It should be stressed that the type-II TW is a stable attractor when  $2.23 < E_b < 2.52$  at  $L = 5$  and numerical simulation confirms that type-II TWs rather than RPOs are observed in this range. For type-II TWs, figure 7(a,b) show that the type-II TWs become unstable to an oscillatory mode for  $E_b > 2.52$ . Hence, for  $L = 5$ , RPOs may be born from the instability of either type-I or type-II TWs for  $E_b > 2.52$ .

For the  $E_b$  where there are oscillations, time series of the energy norm  $\mathcal{E}$  are found to be periodic, implying the existence of RPOs. Using a snapshot of  $S(z, t_0)$  at some  $t_0$  from the numerical simulations as initial guess for our Newton–Krylov code, an exact RPO solution can be obtained. Typical profiles of the RPOs at  $L = 4$  are shown in figure 9(a,b). A spatio-temporal diagram of the film radius  $h$  in figure 9(c) illustrates the oscillating behaviour for two different sized droplets. A more clear picture of the oscillation can be seen in our supplemental video. The dynamics of the RPOs is projected into the  $\mathcal{I} - \mathcal{D}$  vs.  $\mathcal{D}$  plane in figure 10(a). TWs are fixed points on the horizon axis  $\mathcal{I} = \mathcal{D}$ , while RPOs

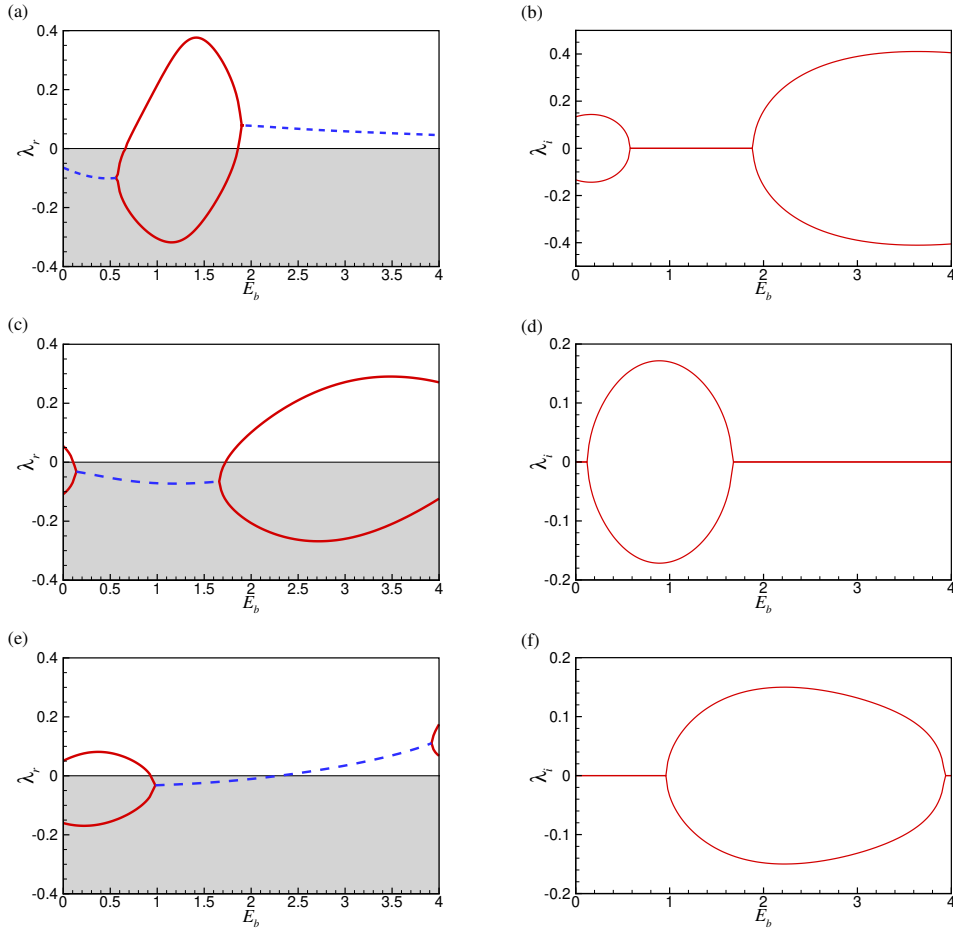


FIGURE 6. Eigenvalue of the type-I TWs vs. the electric number  $E_b$  at (a,b)  $L = 4$ ; (c,d)  $L = 4.5$  and (e,f)  $L = 5$ . The red solid/blue dashed lines represent the stationary/oscillatory mode. For  $L = 5$ , the stability of the lower branch of type-I TW is investigated in (e,f).

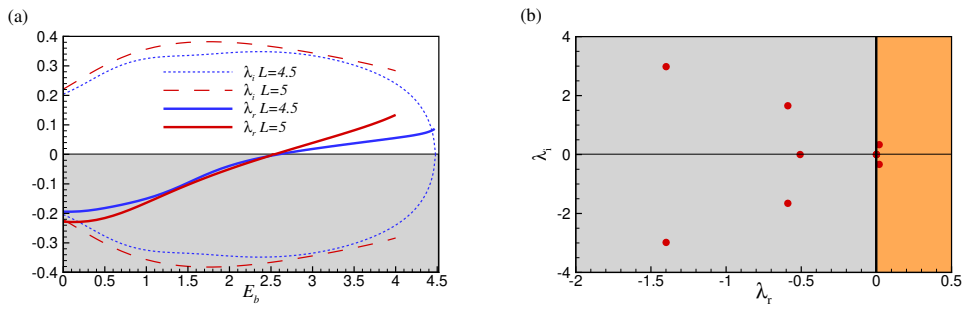


FIGURE 7. (a) Leading eigenvalue for type-II TWs vs. the electric number  $E_b$  at  $L = 4.5, 5$ . The leading mode is oscillatory. (b) The spectra of the eigenvalue problem of type-II TW at  $E_b = 3$ ,  $L = 4.5$ , and two unstable eigenvalues were detected.

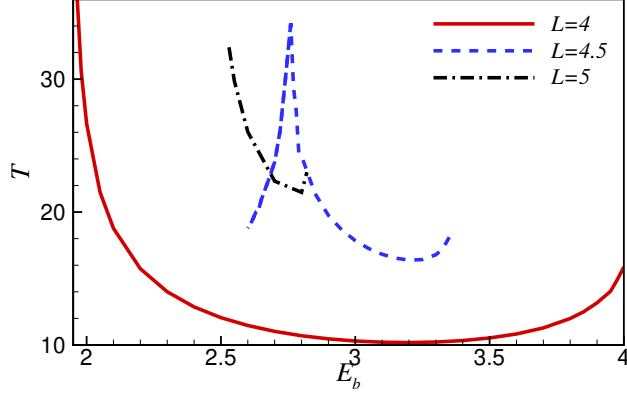


FIGURE 8. The periods of RPOs vs. the electric Weber number at different domain sizes  $L = 4, 4.5, 5$ .

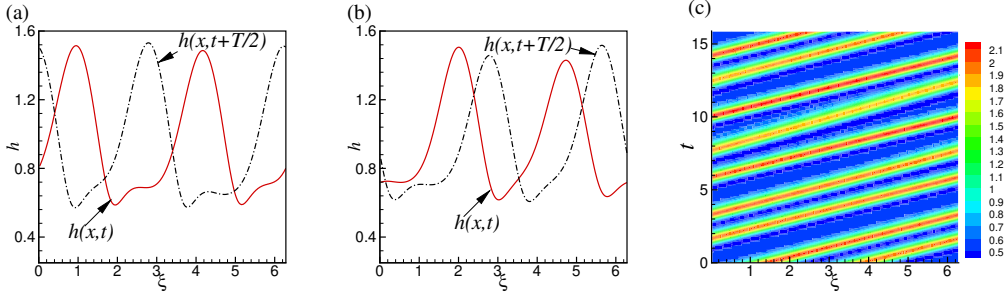


FIGURE 9. (a,b) The interfacial profiles at times  $t$ ,  $t + T/2$  and  $t + T$ . The electric number and time period in (a),(b) are respectively  $(E_b = 2, T = 26.6521, l = 0.4520)$  and  $(E_b = 3, T = 10.2997, l = -0.9633)$ . (c) The space-temporal diagram of  $h(x, t)$  in a period at  $E_b = 4$ . Here, the coordinate  $\xi = \frac{2\pi}{L}z$  and  $L = 4$ .

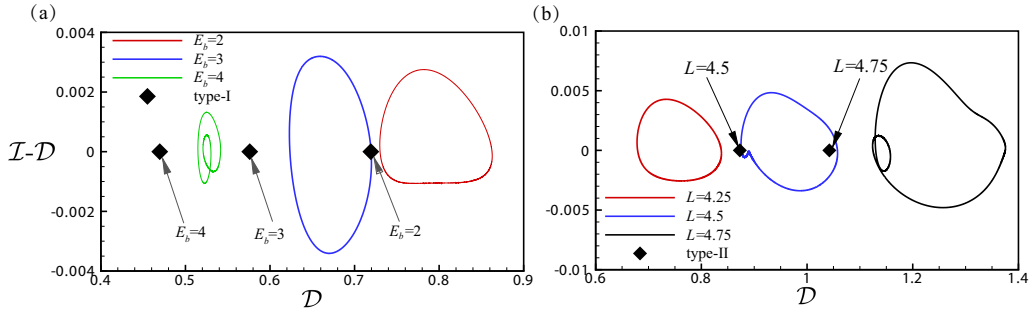


FIGURE 10. RPOs in the  $\mathcal{I} - \mathcal{D}$  vs  $\mathcal{D}$  plane at (a)  $L = 4$ , (b)  $E_b = 3$ . Diamond points are steady TW solutions.

are closed loops that cross this axis. For  $L = 4$ , using a parametric continuation method, RPOs are found for  $E_b$  up to  $E_b \approx 4$ . Further increasing in  $E_b$  leads to the formation of the spike-like structure. When the length of the computational domain is increased for fixed  $E_b = 3$ , RPOs are found up to around  $L = 4.75$ , shown in figure 10(b). Further increasing  $L$  also leads to formation of the spike-like structure.

The period of the RPOs,  $T$ , is plotted against the electric Weber number  $E_b$  in figure 8(a). The electric field has dual effects on the oscillation. For  $L = 4, 5$ , the oscillation becomes faster ( $T$  decreases) as  $E_b$  increases initially. However, beyond some critical point, the oscillation becomes slower ( $T$  increases). For  $L = 4.5$ , the dynamics is a bit more complicated. The oscillation becomes slower ( $T$  increases) as  $E_b$  increases from the bifurcation point  $E_b \approx 2.6$ . Then, the oscillation becomes faster ( $T$  decreases) as  $E_b > 2.78$ . However, as  $E_b$  increases further, the oscillation becomes slower ( $T$  increases). Referring to figure 4(b-d), the RPO runs faster/slower when the oscillation is slower/faster. The RPO is slower than the type-I TW, which might be faster than type-II TW (see figure 4(c) and 15(b)).

For  $L = 4$ , as  $E_b$  is reduced towards 1.94 we find that  $T \rightarrow \infty$  and our Newon-GMRES code stops converging, due to the break down of the linearisation (3.7) for large  $T$ . We are able to get to sufficiently large  $T$ , however, to identify that the RPO connects to the type-I TW. The divergence of  $T$  is in agreement with the linear stability analysis where  $\lambda_i \rightarrow 0$  as  $E_b \rightarrow 1.94^+$  (figure 6(b)). For  $L = 4.5$ , a Hopf bifurcation occurs at  $E_b \approx 2.6$  for the type-II TW (figure 7(a)). The eigenvalue at the bifurcation point  $E_b = 2.6$  predicts a period  $T = 2\pi/\lambda_i = 2\pi/0.34 \approx 18.48$ . The RPO branch is quite contorted as it approaches the type-II branch, but at the last points computed on the branch, the period of the RPO is  $\approx 18.70$  and decreasing, in good agreement with the linear stability calculation. For  $L = 5$ , we have been unable to identify a connection between the RPO and the TWs (see figure 4(d)), as far as we are able to reliably perform the calculations.

To summarise the results in this section, the solution regimes are constructed in figure 3, and in particular, the oscillatory bound states are represented by RPOs. We have demonstrated that the two large droplets cannot survive in a steady bound state but in an oscillatory bound state when  $E_b$  exceeds a critical value (e.g.  $E_b = 2$  and see figure 5(a)). It indicates that we may expect to see steady travelling waves, relative periodic solutions or spike-like structures in experimental study, depending on the strength of electric field and droplet spacing. When the electric field is weak, we should observe the formation of steady liquid viscous bead train due to the Rayleigh-Plateau mechanism. The steady wave train will lose stability and an the oscillating state will emerge as the strength of electric field increases. The spike-like structure should appear when the electric field is strong.

#### 4.2. Invariant solutions in a non-electrified film

In the absence of an electric field, it is observed that droplets can either move in a stable or unstable bound state (Duprat *et al.* 2007), but this oscillation is different from that discussed in §4.1 – here, experimental and numerical studies have shown that the oscillation is caused by the interaction between a large droplet and a much smaller droplet (Craster & Matar 2006; Duprat *et al.* 2007). The large droplet eats small droplets, which can then break up into small droplets. Such a process is cyclical, and we will demonstrate that it can be represented by RPOs.

Space-time diagrams at  $L = 12$  are shown in figure 11. Actually, for  $L = 12$ , other types of solutions do exist, e.g. a one-droplet solution, a three-droplet solution, and so on. The multi-droplets solutions can be stable or unstable bound states. Here we only consider two big droplets in the computational domain so as to isolate the oscillation dynamics. The leading eigenvalues of type-I and type-II TWs are tracked against the domain size  $L$ , shown in figure 12. Results in figure 12(a) show that type-II TWs are stable when  $L \lesssim 6.7$ . Type-I TWs are unstable when  $4.4 \lesssim L \lesssim 5.2$  or  $L \gtrsim 6.3$ . However, type-I TWs do not lose stability to RPOs when  $4.4 \lesssim L \lesssim 5.2$ , as  $\lambda_i = 0$ . Figure 12(a,b)

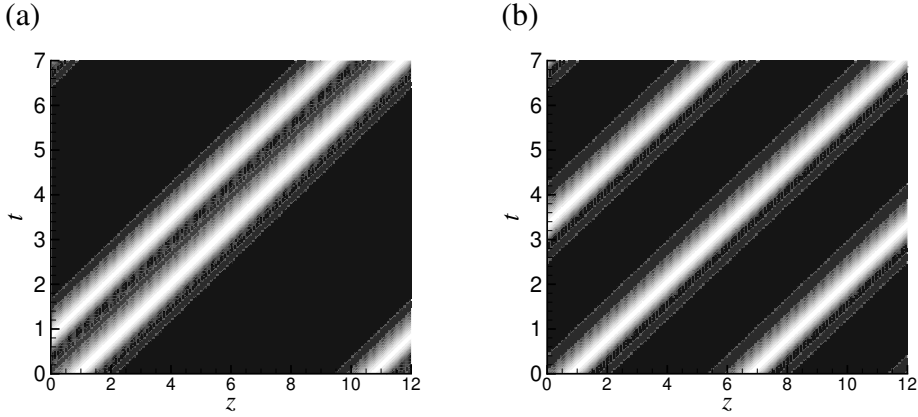


FIGURE 11. The space-time diagram for type-II TW (a), and type-I TW (b). The bright/dark shading indicates elevated and depressed regions. The dependent parameters are  $Bo = \epsilon = 0.2$ ,  $\alpha = 0.25$ ,  $L = 12$ .

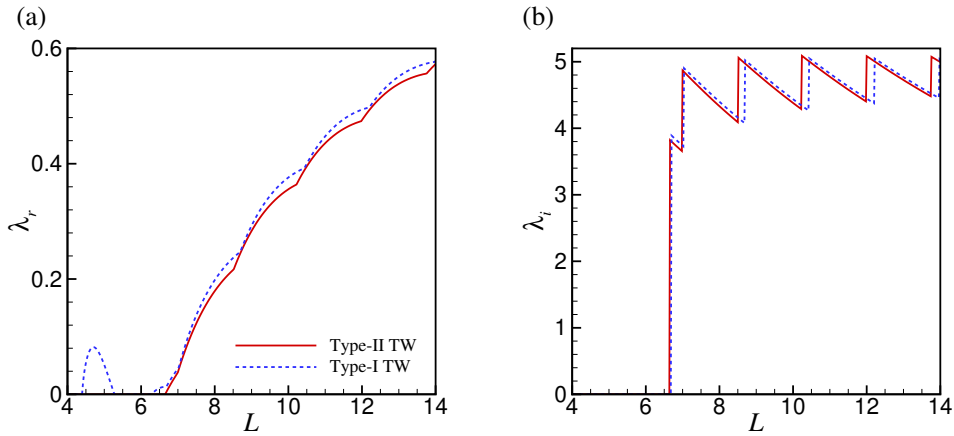


FIGURE 12. (a,b) The leading eigenvalue vs. the domain size for type-I, type-II TWs. The dependent parameters are  $Bo = \epsilon = 0.2$ ,  $\alpha = 0.25$ .

demonstrate that the most unstable modes are oscillatory when  $L \gtrsim 6.7$  for both type-I and type-II TWs, suggesting the existence of RPOs. Interestingly, the sawtooth  $\lambda_i - L$  curve originates from the mode switching in the system: the growth rate  $\lambda_r$  of higher frequency modes increases faster than that of the low frequency modes, leading to the switching. Therefore, the frequency of most unstable mode jumps as  $L$  increases, leading to the sawtooth structure of the  $\lambda_i - L$  curve.

Numerical simulations were performed in order to obtain initial guesses for the RPOs. We fixed  $L = 12$  and obtained three converged exact RPOs, namely RPO1, RPO2, RPO3, whose space-time diagrams are shown in figure 13. We expect that it is possible to find more RPOs of longer period, but we have not pursued this in the present study. The profiles of the three RPOs at some instants in time are shown in figure 14(b). For RPO1, between the two main big droplets, the film is unstable and develops into a ripple-like structure. For RPO2, the unstable film between the two main droplets evolves into two small droplets. For RPO3, there are three small droplets between the two main droplets.

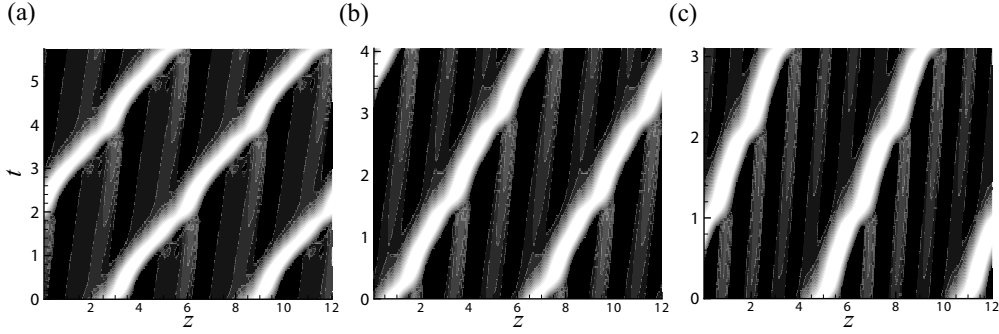


FIGURE 13. The space-time diagrams for the RPOs plotted in three periods at  $L = 12$ . (a) RPO1 with period  $T = 1.9122$ ; (b) RPO2 with period  $T = 1.3501$ ; (c) RPO3 with period  $T = 1.0344$ . The dependent parameters are  $Bo = \epsilon = 0.2$ ,  $\alpha = 0.25$ .

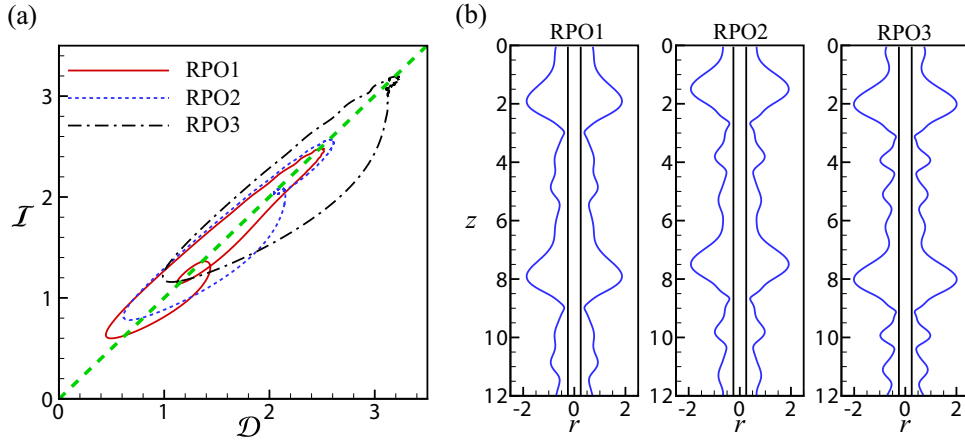


FIGURE 14. (a) Three exact RPOs in the  $\mathcal{I}$ - $\mathcal{D}$  plane at  $L = 12$ . (b) The instant profiles of the liquid films for the RPOs. The dependent parameters are  $Bo = \epsilon = 0.2$ ,  $\alpha = 0.25$ . Three movies for these RPOs are shown in the supplementary materials. Each movie shows three periods of the RPO.

As there are more small droplets between the two main droplets, the mean distance between the big droplet and its nearby small droplet decreases. Therefore, it takes less time for the big droplet to consume the nearby small droplet and the oscillation becomes faster, i.e. the periods decrease from RPO1 to RPO3 (see figure 15(a)). We observe that the big droplet eats the front small droplet or ripple and itself is unstable at the rear region which breaks up into new ripples or small droplets. The breakup of big droplet at its rear region is due to the Plateau-Rayleigh mechanism. Such a cycle process (also confirmed in figure 14(a)) is self-sustaining, which gives the birth of exact RPOs in the non-electrified film.

It is interesting to investigate how the period and wave speed of the RPO depend on the domain size. Figure 15(a) shows that the period  $T$  becomes longer as the domain size  $L$  increases. We speculate that this is because the distance between big droplet and its front small droplet (the closest one to the big droplet) becomes larger, and therefore longer time is required for the coalescence process. The domain sizes of the three observed different flow regimes in Kliakhandler *et al.* (2001) are within the current computation, and we do not investigate longer domains in the present study.

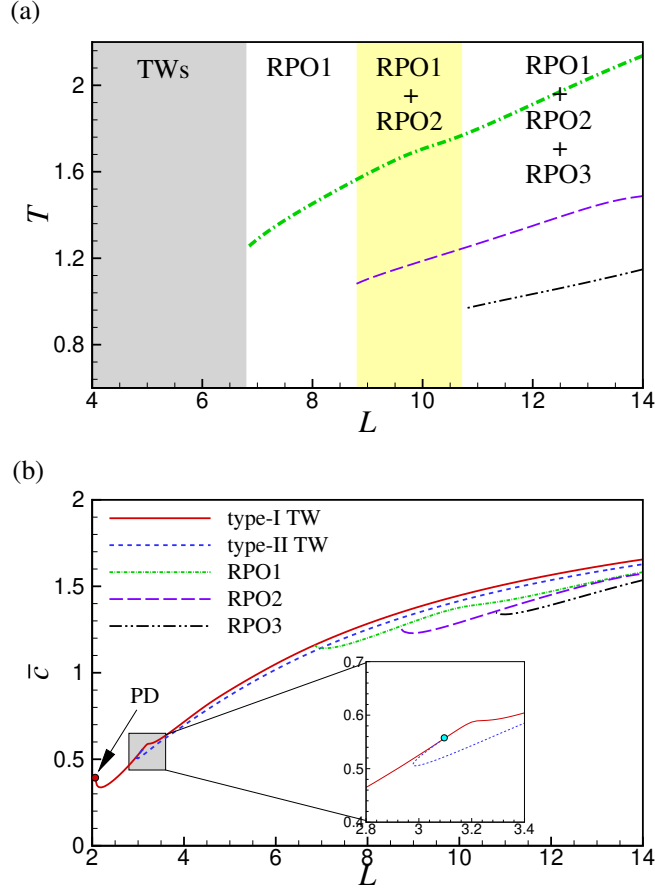


FIGURE 15. (a) Period  $T$  vs. the domain size  $L$  for RPOs. Solutions of different regimes are illustrated. When  $L < 6.85$ , only TWs are detected. RPO1 is detected when  $L > 6.85$ ; RPO2 is detected when  $L > 8.7$  and RPO3 is detected when  $L > 10.7$ . (b) The wave speed vs. the domain size  $L$ . The dependent parameters are  $Bo = \epsilon = 0.2$ ,  $\alpha = 0.25$ . PD stands for period doubling bifurcation.

Different solution regimes are shown in figure 15(a). RPO1 is not detected when  $L < 6.85$ . The curve for RPO1 in figure 15(b) connects with the type-I TW solution at  $L \approx 6.85$ . We have verified that the spatial form for RPO1 is very similar to the type-I TW at  $L = 6.85$ , where the ripple between the two big droplets is very small. This indicates that RPO1 is born from the instability of the type-I TW, and explains why we do not detect RPO1 below  $L = 6.8$ . RPO2, RPO3 were not detected for  $L \lesssim 8.7, 10.7$  respectively. A possible reason why they do not exist in smaller domains may due to insufficient space for varying numbers of small beads or ripples. The wave speed  $\bar{c}$  reduces for a stronger oscillation (RPO1 is faster than RPO2, and RPO2 is faster than RPO3). As the domain size  $L$  increases, the wave speed of RPOs increases (see figure 15(b) and figure 16(c)). This is because the average height of the large droplet increases and therefore a faster wave (Craster & Matar 2006). When the domain size is large, although these RPOs can be tracked using numerical continuation, they lose stability and the system is typically chaotic, hence we expect a host of RPOs to describe the droplet coalescence and breakup processes discussed by Craster & Matar (2006). A selection of the shortest

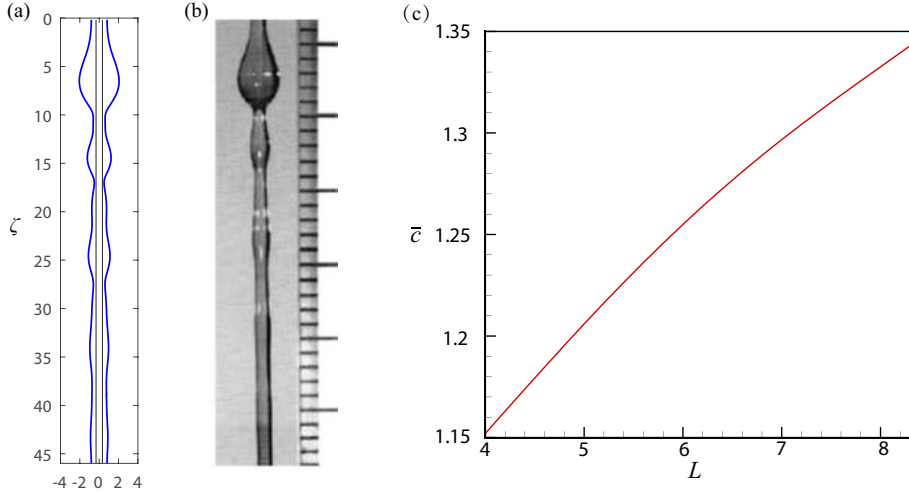


FIGURE 16. (a) A snapshot of exact RPO. (b) Regime “c” adapted from Kliakhandler *et al.* (2001). The axis in (a) is rescaled  $\zeta = z/\epsilon$  so as to compare with the experimental observation. (c) Wave speed of the RPO vs. domain size, in which there is only one big droplet. A video for the RPO in the supplemental material demonstrates the unsteady flow. The dependent parameters  $\epsilon = 0.178$ ,  $\alpha = 0.3262$ ,  $L = 8.185$  for regime “c” were taken from Craster & Matar (2006).

orbits, however, is expected to be sufficient to capture most of the dynamics (Budanur *et al.* 2017).

Finally, we revisit the experimental study of the flow regime “c” in Kliakhandler *et al.* (2001), where there is a large droplet with some small ripples at its front. In contrast to the “steady” flow regime “b”, the flow regime “c” is an essentially unsteady state due to the droplet coalescence and breakup process Craster & Matar (2006). Although the TW solution excellently captures the dynamics of flow regime “b”, it is questionable whether or not we can compare a “steady” TW with flow regime “c”. Craster & Matar (2006) observed that the large droplet oscillates in the experiment and proposed that flow regime “c” is a superposition of a steady TW and small perturbations. However, their numerical experiment does not compare well with the experimental study, not only in the wave speed but also in the wave profile. In Ruyer-Quil *et al.* (2008), the streamwise dissipation effect was considered, which leads to a smaller wave speed ( $c = 0.94$ ) than Craster & Matar (2006). Novbari & Oron (2009) used an energy integral model and predicted a bit higher phase speed than Craster & Matar (2006),  $c = 1.48$ , and the streamwise dissipation effect was neglected by them (The wave speeds by Ruyer-Quil *et al.* (2008); Novbari & Oron (2009) are rescaled by  $W = \rho h_0^2 g / \mu$  here.). Indeed, Novbari & Oron (2009) has realized that flow regime “c” is not a TW because it was unsteady, although they compared it with a TW. All these TWs, however, do not capture a correct film profile: there are no small beads co-existing with the large droplet. Within our set of periodic orbits we have found profiles of the film very much like experimental observation, figure 16. It should be stressed here that the small droplets/ripples in the front of the big droplet in figure 16 are captured by the RPO, which are not seen in the TW. Kliakhandler *et al.* (2001) simulated flow regime “c” using their thick film model and showed that these small droplets can survive with big droplets in an unsteady state. The large droplet catches up with and consumes the small droplets in the front, and the rear region of the large droplet breaks up into small droplet. Such a process recurs in the system, i.e. the profile in figure 16(a) appears periodically, which is striking similar

to that in flow regime “c”. Furthermore, the period of the obtained RPO in figure 16(a) is  $T = 1.7156$ . However, no experimental study on RPOs in this film flow was reported, and the period of flow regime “c” in experiments remains unknown. The wave speed of this RPO  $\bar{c} = 1.34$  is a little smaller than the wave speed of the TW,  $c = 1.36$  (Craster & Matar 2006), and is closer to the experimental observation  $c = 0.93$ . Hence, the RPO captures the dynamical scenario, i.e. oscillation, the wave speed of flow regime “c”, and the film profile better than the steady TWs, which provides a better understanding of this unsteady state than the TW solution. The mean wave speed predicted by the RPO, however, is still about 30% higher than the measured one. Note that, the wave speed of flow regime “a” is correctly predicted by Craster & Matar (2006). It can be inferred that the 30% difference is not caused by dropping the inertia term because the Reynolds number in flow regime “c” is much smaller than in flow regime “a”. As is shown by Ruyer-Quil *et al.* (2008), the streamwise viscous dissipation effect can significantly improve the prediction of the wave speed of steady TWs. This suggests that the streamwise diffusion is important when the Reynolds number is small, which is the reason why the predicted wave speed by the asymptotic model is higher than the experimental value.

## 5. Conclusions

We have investigated a perfectly-conducting liquid film flowing down a vertical fibre subject to a radial electric field. The dynamics of the liquid film was examined using a long-wave model. The dynamical systems approach was employed to extract recurrent solutions, i.e. travelling waves (TWs) and relative periodic solutions (RPOs). The Newton–Krylov-hookstep method was used to find the RPOs presented in this paper. Two cases were discussed: an electrified film and a non-electrified film.

For the case with an electric field, we investigated the interactions between two big droplets. Numerical simulation showed that the system can evolve into a steady TW state when the electric field is weak. Steady TW solutions, either in the form of two identical droplets (type-I TW) or two slightly different droplets (type-II TW) were tracked. Linear stability analysis shows that the TW solutions become unstable as the electric field exceeds some threshold, and oscillatory instabilities of the TWs develop into RPO solutions. In the oscillatory state, the two droplets are slightly different in size, while two identical droplets do not cause an oscillation unless they are unstable. Interestingly, RPOs were also found through the instability of steady TW solutions in an electrified liquid film flowing down an inclined plane very recently (Lin *et al.* 2018).

We have also demonstrated that electric field has dual effects on the oscillation: the oscillation can be accelerated or decelerated by the electric field. When the electric field is strong, the two droplets merge together, leading to spike-like singular structure.

When the electric field is turned off, several RPOs were found in the non-electrified film. Indeed, steady TWs are also unstable when the domain size exceeds a critical value. RPOs are then found after the instability of the steady TWs. Interestingly, the RPO represents the self-sustaining droplet coalescence and breakup process. The periods and wave speeds of RPOs increase as the domain size increases. An interesting observation is that the wave speed of RPO is lower than the type-I TW, and the motion of droplets is slowed down by the oscillation, no matter if the electric field is imposed or removed.

In addition, the RPO captures well not only the dynamical scenario, but also captures the temporal variation of the wave speed. We find a snapshot of the RPO solution remarkably similar to experimental observation. Together, our results indicates that the RPO provides a better model of the unsteady flow regime in the film flow than steady TW solution.

ZD and APW acknowledge support from an EPSRC grant *optimization in fluid mechanics EP/P000959/1*. ZD also acknowledges Prof. R.R. Kerswell and Dr. Jacob Page for their kind help on the Newton–Krylov-hookstep method in Chandler & Kerswell (2013), which is crucial for the computation of the relative periodic orbits in this study. ZD and APW also appreciate the three anonymous referees for their many insightful comments, which help us to improve the paper significantly.

## REFERENCES

- BUDANUR, N., SHORT K., FARAZMAND M. & WILLIS A. Relative periodic orbits form the backbone of turbulent pipe flow. *J. Fluid Mech.* **833**, 274-301.
- BLYTH M.G., TSELUIKO D., LIN T.-S. & KALLIADASIS S. 2018 Two-dimensional pulse dynamics and the formation of bound states on electrified falling films. *J. Fluid Mech.* **855**, 210-235.
- CHANDLER, G. & KERSWELL R. 2013 Invariant recurrent solutions embedded in a turbulent two-dimensional Kolmogorov flow. *J. Fluid Mech.* **722**, 554-595.
- CHANTRY, M., WILLIS, A. & KERSWELL R. 2014 Genesis of streamwise-localized solutions from globally periodic travelling waves in pipe flow. *Phys. Rev. Lett.* **112**, 164501.
- CHANG C. & DEMEKHIN E. 1999 Mechanism for drop formation on a coated vertical fibre. *J. Fluid Mech.* **380**, 233.
- CONROY D., MATAR O., CRASTER R. & PAPAGEORGIOU D. 2011 Breakup of an electrified perfectly conducting, viscous thread in an AC field. *Phys. Rev. E* **83**, 066314.
- CRASTER R. & MATAR O. 2005 Electrically induced pattern formation in thin leaky dielectric films. *Phys. Fluids* **17** (3), 032104.
- CRASTER R. & MATAR O. 2006 On viscous beads flowing down a vertical fibre. *J. Fluid Mech.* **553**, 85-105.
- CRASTER R. & MATAR O. 2009 Dynamics and stability of thin liquid films. *Rev. Mod. Phys.* **81**, 1131-1198.
- CVITANOVIĆ, P., DAVIDCHACK, R. & SMINOS, E. 2010 On the state space geometry of the Kuramoto–Sivashinsky flow in a periodic domain. *SIAM J. Applied Dynamical Systems* **9**, 1-33.
- CVITANOVIĆ, P. & GIBSON J. 2010. Geometry of the turbulence in wall-bounded shear flows: periodic orbits, *Phys. Scr. T* **142**, 014007.
- DE RYCK A. & QUÉRÉ D. 1996 Inertial coating of a fiber. *J. Fluid Mech.* **311**, 219-237.
- DING Z., XIE J., WONG T.N. and LIU R. 2014 Dynamics of liquid films on vertical fibres in a radial electric field. *J. Fluid Mech.* **752**, 66.
- DING Z. and WONG T.N. 2017 Three-dimensional dynamics of thin liquid films on vertical cylinders with Marangoni effect. *Phys. Fluids* **29**, 1.
- DUPRAT C., RUYER-QUIL C., KALLIADASIS S. & GIORGIUTTI-DAUPHINÉ F., 2007 Absolute and convective instabilities of a viscous film flowing down a vertical fiber. *Phys. Rev. Lett.* **98**, 244502.
- Duprat C., Giorgiutti-Dauphiné F., Tseluiko D., Saprykin S. & Kalliadasis S. 2009 Liquid film coating a fiber as a model system for the formation of bound states in active dispersive-dissipative nonlinear media. *Phys. Rev. Lett.* **103**, 234501.
- FRENKEL A. 1992 Nonlinear theory of strongly undulating thin films flowing down vertical cylinders. *Europhys. Lett.* **18**, 583-588.
- KLIAKHANDLER I., DAVIS S. & BANKHOFF S. 2001 Viscous beads on vertical fibre. *J. Fluid Mech.* **429**, 381-390.
- KALLIADASIS S. & CHANG C. 1994 Drop formation during coating of vertical fibres," *J. Fluid Mech.* **261**, 135.
- KALLIADASIS S., RUYER-QUIL C., SCHEID B. and VELARDE M.G. 2012 *Falling Liquid Films*, Springer London.
- LIN T.-S., TSELUIKO D., BLYTH M.G., KALLIADASIS S. 2018 Continuation methods for time-periodic traveling-wave solutions to evolution equations. *Applied Mathematics Letters*, **86**, 291-297.

- LIU R., CHEN X. & DING Z. 2018 Absolute and convective instabilities of a film flow down a vertical fiber subjected to a radial electric field. *Phys. Rev. E*, **97**, 013109.
- NOVBARI E. & ORON A. 2009 Energy integral method model for the nonlinear dynamics of an axisymmetric thin liquid film falling on a vertical cylinder. *Phys. Fluids* **21**, 062107.
- ORON, A., DAVIS, S. H. & BANKOFF, S. G. 1997 Long-scale evolution of thin liquid films. *Rev. Mod. Phys.* **69**, 931-980.
- PAPAGEORGIOU D. 2018 Film flows in the presence of electric fields. *Annu. Rev. Fluid Mech.* **51**, 155.
- PRADAS M., TSELUIKO D. & KALLIADASIS S. 2011 Rigorous coherent-structure theory for falling liquid films: Viscous dispersion effects on bound-state formation and self-organization. *Phys. Fluids* **23**, 044104.
- QUÉRÉ D. 1999 Fluid coating on a fiber. *Annu. Rev. Fluid Mech.* **31**, 347-384.
- RUYER-QUIL C. & MANNEVILLE P. 1998 Modeling Film flows down inclined planes. *Eur. Phys. J. B* **6**, 277-292.
- RUYER-QUIL C., TREVELEYAN P., GIORGIUTTI-DAUPHINÉ F. & KALLIADASIS S. 2008 Modeling film flows down a fibre. *J. Fluid Mech.* **603**, 431-462.
- SAVILLE, D. A. 1997 Electrohydrodynamics: the Taylor-Melcher leaky dielectric model. *Annu. Rev. Fluid Mech.* **29**, 27-64.
- SADEGHPOUR A., ZENG Z. & JU Y. 2017 Effects of nozzle geometry on the fluid dynamics of thin liquid films flowing down vertical strings in the Rayleigh-Plateau regime. *Langmuir*, **33**, 6292-6299.
- SCHÄFFER E., THURN-ALBRECHT T., RUSSELL T. and STEINER U., Electrically induced structure formation and pattern transfer. *Nature* **403**, 874, 2000.
- SHKADOV V. YA., BELOGLAZKIN A. & GERASIMOV S. 2008 Solitary waves in a viscous liquid film flowing down a thin vertical cylinder. *Mosc. Univ. Mech. Bull.* **63**, 122-128.
- SISOEV G., CRASTER R., MATAR O. & GERASIMOV S. 2006 Film flow down a fibre at moderate flow rates. *Chem. Eng. Sci.* **61**, 7279-7298.
- TRIFONOV YU. YA. 1992 Steady-State travelling Waves on the Surface of a Viscous Liquid Film Falling Down on Vertical Wires and Tubes. *AIChE J.* **38**, 821-834.
- WANG Q. & PAPAGEORGIOU D. 2011 Dynamics of a viscous thread surrounded by another viscous fluid in a cylindrical tube under the action of a radial electric field: breakup and touchdown singularities. *J. Fluid Mech.* **683**, 27-56.
- WRAY A., MATAR O. & PAPAGEORGIOU D. 2012 Nonlinear waves in electrified viscous film flow down a vertical cylinder. *IMA J. Appl. Math.* **77**, 430-440.
- WRAY A., PAPAGEORGIOU D. & MATAR O. 2013 Electrified coating flows on vertical fibres: enhancement or suppression of interfacial dynamics. *J. Fluid Mech.* **735**, 427-456.
- WRAY A., PAPAGEORGIOU D. & MATAR O. 2013 Electrostatically controlled large-amplitude, non-axisymmetric waves in thin film flows down a cylinder. *J. Fluid Mech.* **736**, R2.
- VISWANATH D. 2007 Recurrent motions within plane Couette turbulence. *J. Fluid Mech.* **580**, 339-358.
- ZENG Z., SADEGHPOUR A., WARRIER G. & JU Y. 2017 Experimental study of heat transfer between thin liquid films flowing down a vertical string in the Rayleigh-Plateau instability regime and a counterflowing gas stream. *Int. J. Heat Mass Trans.* **108**, 830-840.